Decoupling early-stage cracking and propagation mechanisms in liquid metal embrittlement of Zn-galvanised TWIP steel

Bertolo, Virgínia; Mahadevan, Gautham; de Kloe, René; Petrov, Roumen H.; Popovich, Vera

DOI
10.1016/j.jmrt.2025.08.055

Publication date
2025

Document Version
Final published version

Published in
Journal of Materials Research and Technology

Journal of Materials Research and Technology 38 (2025) 1617–1632

Contents lists available at ScienceDirect

Journal of Materials Research and Technology

journal homepage: www.elsevier.com/locate/jmrt

Decoupling early-stage cracking and propagation mechanisms in liquid metal embrittlement of Zn-galvanised TWIP steel

Virgínia Bertolo [a,b,*], Gautham Mahadevan [a,b], René de Kloe [c], Roumen H. Petrov [b], Vera Popovich [a]

[a] Department of Materials Science and Engineering, Delft University of Technology, Mekelweg 2, 2628 CN, Delft, the Netherlands
[b] Department of Electromechanical, Systems and Metals Engineering, Ghent University, Technologiepark 131, B-9052, Ghent, Belgium
[c] EDAX-Gatan, AMETEK BV, Ringbaan Noord 103, 5046 AA, Tilburg, the Netherlands

ARTICLE INFO

Handling editor: SN Monteiro

Keywords:
Liquid metal embrittlement
Fracture onset
Micromechanisms
Zn-galvanised
TWIP steel
Interrupted testing

ABSTRACT

Liquid metal embrittlement (LME) presents a major barrier to the widespread adoption of advanced high-strength steels in automotive applications. Despite extensive research, decoupling its early-stage cracking and propagation micromechanisms remains challenging and is a key research gap. Distinguishing these stages is crucial to understanding the conditions and factors that are favourable for LME and to developing mitigation strategies. Moreover, it can improve the accuracy of predictive models through detailed knowledge from initiation to propagation. In this study, this challenge is addressed by performing interrupted Gleeble hot tensile tests on a Zn-galvanised twinning-induced plasticity steel, simulating resistance spot welding conditions. This approach enables tracking LME progression under applied stress and identifying fracture micromechanisms at early and advanced stages of cracking. Additionally, existing theories on LME micromechanisms are often contradictory, highlighting the need for fundamental research in this area. The findings reveal that LME begins with the contact between liquid Zn and the substrate, leading to Zn diffusion into the substrate by diffusion-induced grain boundary migration and dissolution of the substrate by erosion-corrosion. This dissolution generates defects on the substrate and facilitates Fe diffusion into liquid Zn. Subsequently, defects are filled with liquid and the Zn-rich defect tips, connected to grain boundaries, enhance Zn grain boundary diffusion and weaken intergranular cohesion. Under tensile stress, these weakened boundaries decohere and lead to crack nucleation. Newly formed crack surfaces allow fresh Fe-rich liquid Zn to penetrate, continuing the process until fracture. Future work will focus on the influence of microstructure on LME crack growth.

1. Introduction

The shift from conventional high-strength steel to advanced high-strength steel (AHSS) offers the opportunity to create lighter and stronger vehicles, leading to enhanced safety, reduced material consumption, and improved fuel efficiency. Consequently, waste and CO_2 emissions are reduced. Among AHSS options, high-manganese twinning-induced plasticity (TWIP) steels are particularly promising for the automotive industry due to their exceptional balance of strength, toughness, and high work-hardening rates [1]. However, despite their benefits, AHSS, especially austenitic grades, are highly susceptible to liquid metal embrittlement (LME) [2–4]. This susceptibility represents a significant challenge to progressing towards a future with a greener, safer, and more efficient automotive sector.

LME is characterised by ductility loss of solid-liquid metal couples (e.g., Zn–Fe, Al–Ga, and Ni–Bi) triggered by the simultaneous action of high temperature and tensile stress [5–8]. For instance, in the automotive industry, LME often happens during resistance spot welding, performed thousands of times in the vehicles' assembly. At high temperatures, the anti-corrosion Zn coating melts and penetrates through the steel grain boundaries, leading to decohesion, which, along with the weld's residual tensile stresses, assists in cracking, leading to material embrittlement. However, this explanation provides a general and simplified understanding of LME, and numerous theories to elucidate LME micromechanisms have been developed in the past decades.

The most well-accepted LME models in the Fe–Zn system are the brittle fracture Stoloff-Johnson-Westwood-Kamdar (SJWK) and the grain boundary-based ones [9–12]. The SJWK model explains that the

* Corresponding author. Department of Materials Science and Engineering, Delft University of Technology, Mekelweg 2, 2628 CN, Delft, the Netherlands.
E-mail address: v.moretebarbosabertolo@tudelft.nl (V. Bertolo).

https://doi.org/10.1016/j.jmrt.2025.08.055
Received 26 May 2025; Received in revised form 31 July 2025; Accepted 6 August 2025
Available online 7 August 2025

strain-activated adsorption of atoms of liquid Zn at the crack tip of the Fe-based substrate reduces the cohesive strength of grain-to-grain bonds [11,12]. Under sufficiently large tensile stress, the weakened bonds break. As tensile stress and the supply of liquid Zn atoms at the crack tip to freshly created surfaces remain, the process repeats, leading to crack propagation. On the contrary, according to the grain boundary-based models – Gordon-An and Klinger [9,10] – LME crack nucleation and propagation are preceded by stress-assisted diffusion of atoms of liquid Zn through grain boundaries of the Fe-based matrix [9,10]. Gordon-An [9] states that accumulating Zn atoms over a sufficient concentration cracks open the grain boundary. Similarly, Klinger [10] assumes the formation of a diffusion wedge at the grain boundary, resulting in high thermodynamically generated tensile stresses normal to the grain boundary and, finally, grain boundary fracture. In both models, crack propagation occurs through consecutive steps of grain boundary diffusion and crack nucleation.

Studies on LME in TWIP steels [2,13–15] are divided between the abovementioned theories. Lee et al. [13] and Beal et al. [2] suggest that LME results from the sequential infiltration of liquid Zn along austenitic grain boundaries, leading to crack formation along the Zn penetration path, which allows further infiltration. This model aligns with the SJWK mechanism. Conversely, Razmpoosh et al. [15] propose that the initial stage of LME is driven by rapid grain boundary diffusion. As the solubility limit of Zn in austenite is reached, liquid Zn forms, decohering the grain boundary. Subsequently, the LME crack opens, allowing fresh liquid Zn to infiltrate and advance along the crack path, consistent with the Gordon-An model. Kang et al. [14], in turn, suggest that both liquid Zn grain boundary percolation and stress-assisted solid-state grain boundary diffusion models may play a role. As can be noticed, existing theories on LME micromechanisms are contradictory, and the divergence among them highlights the complexity of LME micromechanisms. Moreover, the rapid progression of LME and the limitation of performing *in situ* tests due to the high vapour pressure of Zn prevent experimental verification of LME micromechanisms, particularly in the early cracking stages. Consequently, the phenomenon remains incompletely understood. Since early-stage cracking and crack propagation may involve different chemical and physical processes, by studying them separately, we can better understand the specific conditions and factors that influence each stage and develop targeted strategies to mitigate the LME sensitivity of AHSS. To address these challenges and enable separate analysis of the nucleation and propagation stages, an interrupted approach in welding and hot tensile tests has been proposed.

This study focuses on characterising LME in Zn-galvanised TWIP steel. In addition to its promising application in the automotive industry, twinning-induced plasticity (TWIP) steel offers a single-phase structure with high LME susceptibility that remains stable at elevated temperatures, reducing the complexity of analysing LME mechanisms. An innovative approach was employed using interrupted Gleeble hot tensile testing to simulate resistance spot welding conditions and track LME progression. By applying progressively higher stress levels, the interaction between Zn and the steel microstructure was examined, allowing the identification of micromechanisms active both at early and advanced stages of cracking. This comprehensive understanding of the distinct stages of LME will help enhance the performance and reliability of Zn-galvanised TWIP steel components in service.

2. Materials and methods

2.1. Material

The investigated material was a Zn hot-dip galvanised, fully austenitic TWIP steel. The sheets were 1.23 mm thick with an approximately 12 μm Zn layer. The chemical composition of the steel substrate, measured by X-ray fluorescence (XRF) and LECO combustion analysis, and its tensile properties are presented in Table 1. Fig. 1 (a) presents a scanning electron microscopy (SEM) image and Fig. 1(b–d) its respective energy-dispersive spectroscopy (EDS) maps for Zn, Fe, and Al, showing the flat, flawless interface between the Zn coating and steel substrate, and an interfacial Al-rich layer. Furthermore, Fig. 1 (e) shows the normal inverse pole figure (IPF-ND) of a randomly selected region of the TWIP steel substrate, where the black and red lines represent the high-angle grain boundaries (>15°) and the $\sum$3 boundaries, which constitute about 70 % of the twin boundaries. The grain size of the TWIP steel, excluding coherent $\sum$3 twin boundaries, is 5.4 ± 1.7 μm (used EBSD parameter: max ferret diameter with 15° tolerance angle). The single-phase austenitic microstructure was deliberately chosen for this study to make the investigation of LME micromechanisms in AHSS less complex.

2.2. Gleeble hot tensile tests

Hot tensile tests were performed via the Gleeble thermomechanical simulator to mimic the resistance spot welding process. Aiming to decouple early-stage cracking and propagation micromechanisms, hot tensile tests interrupted at predefined stress levels to capture intermediate LME stages are proposed as the main experimental approach. To define the most interesting test conditions for interrupted hot tensile tests, the susceptibility of the Zn-galvanised TWIP steel to LME and its ductility through the temperature range first need to be understood. Then, samples were first tested up to fracture at 600 °C, 700 °C, and 800 °C, in load control mode at 30 kN/s. Fig. 2 displays the specimens' dimensions and orientation, and the used Gleeble thermomechanical profile. The thermomechanical profile parameters have been selected based on [16] to be representative of welding conditions. According to DiGiovanni and Biro [16], the tensile strain rate should be between 0.1 and 1.0 s^{-1}. In our study, we selected a strain rate of 0.3 s^{-1}. However, since we performed interrupted tensile tests at different load levels, these needed to be executed in load control mode. To ensure consistent deformation conditions between displacement-controlled and load-controlled tests, we first conducted displacement-controlled tests and recorded the corresponding load rate. The resulting load rate of 30 kN/s was found to be equivalent to the displacement rate of 0.3 s^{-1} under our test configuration. One uncoated (not susceptible to LME used as reference material) and two Zn-galvanised TWIP steel samples were tested for each temperature. Zn-galvanised specimens have the Zn coating removed at one of the sides where the thermocouple is welded. The steel samples were stripped of their Zn coating through chemical etching in a 15 % HCl and 2 % hexamethylenetetramine solution, where the surface intended to be nonexposed is protected with duct tape. It is important to mention that the length of the homogeneously heated area has been estimated by placing thermocouples at the centre of the tensile specimen (control thermocouple) and 1 mm, 2 mm, and 3 mm away from the control thermocouple. The temperature difference between the control thermocouple and the ones 1 mm, 2 mm, and 3 mm away was 0 °C, 20 °C, and 60 °C, respectively. This means that the length of the

Table 1
Chemical composition, measured by XRF and LECO, and tensile properties of the studied TWIP steel substrate.

Material TWIP	Fe wt.%	C	Mn	Al	Ni	Cr, S, Si, Ti, P	Yield Strength (MPa)	Tensile Strength (MPa)	Uniform Elongation (%)
	Bal.	0.62 ± 0.01	16.8 ± 0.3	1.30 ± 0.02	0.5 ± 0.01	0.24 ± 0.02	435	900	54

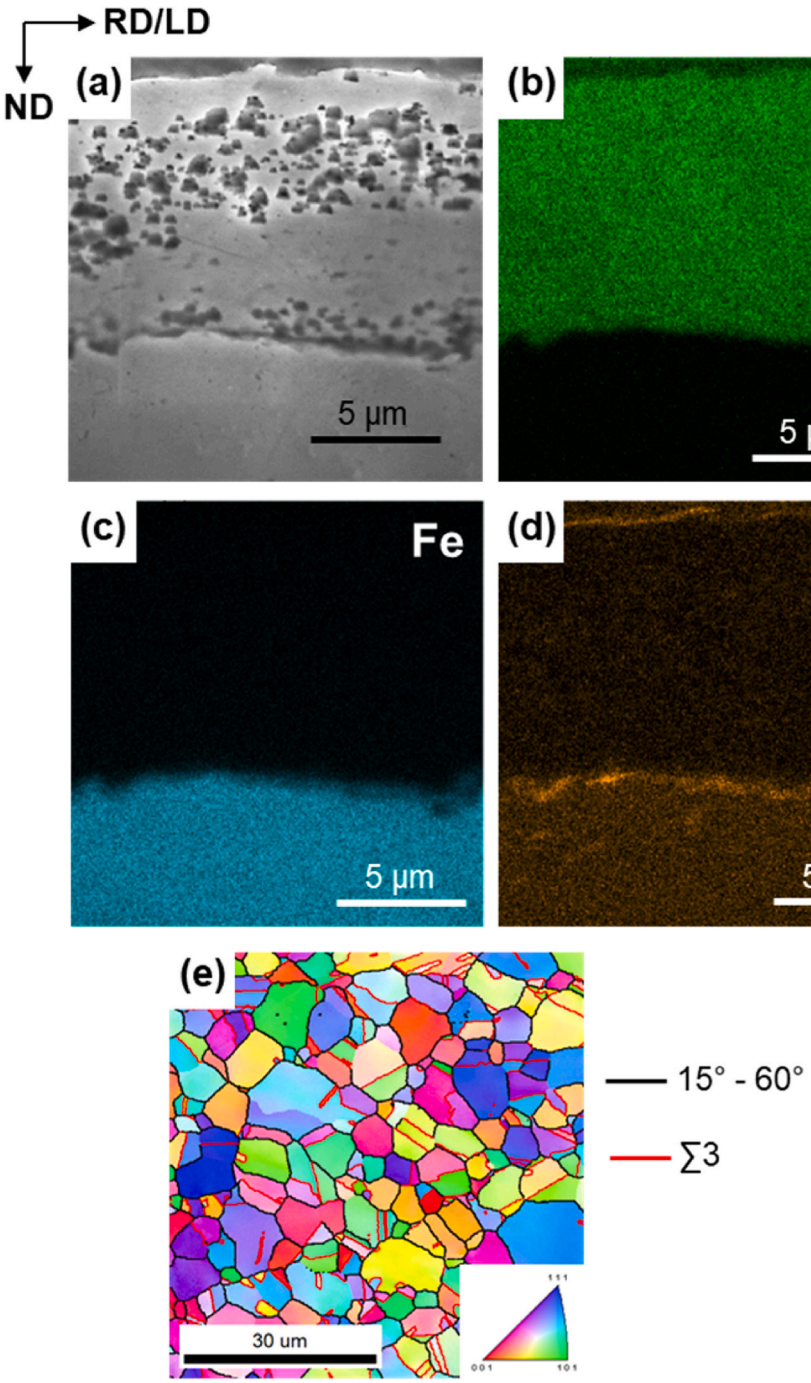

Fig. 1. (a) SEM micrograph of the Zn-galvanised TWIP steel. (b–d) EDS elemental maps for Zn, Fe, and Al, respectively, of area (a) highlighting the Zn-rich coating, Fe-rich substrate, and an interfacial Al-rich layer. (e) IPF-ND map of a randomly selected region of the TWIP steel substrate, where high-angle grain boundaries (15°–60°) are indicated by black lines and ∑3 twin boundaries by red lines. RD, LD, and ND denote rolling, loading, and normal directions, respectively.

specimen subjected to homogenous conditions is 2 mm (considering a symmetrical temperature distribution on both the right and left sides of the control thermocouple), and further study will focus on the areas within this range.

By comparing the displacement of uncoated and coated samples, it has been observed a progressive loss of ductility with the increase in temperature: 10 %, 50 %, and 80 % at 600 °C, 700 °C, and 800 °C, respectively. While at 600 °C, the material is barely affected, the Zn-galvanised TWIP steel is dramatically embrittled at 800 °C. Hence, interrupted hot tensile tests were carried out at 800 °C to evaluate the material in its highest state of susceptibility to LME. Based on the stress–stroke curves at 800 °C (Fig. 3(a)), four stress levels, namely S1, S2, S3, and S4, were selected. These levels represent different stages of material behaviour: S1 (90 MPa) lies in the elastic regime, corresponding to 0.78 of the yield stress (δ_y); S2 (140 MPa) is in the plastic regime, just after the yield point at 1.22 δ_y; S3 (170 MPa) is also in the plastic regime, far above the yield point at 1.48 δ_y; and S4 (175 MPa) is near fracture, at 1.52 δ_y. The stress–stroke curve in Fig. 3 (a) displays slight oscillations, which result from Gleeble's thermal and force control feedback loop. These minor fluctuations remain in a narrow range and do not interfere with the validity of the mechanical data. The theoretical thermomechanical test profile for interrupted tests is shown in Fig. 3 (b).

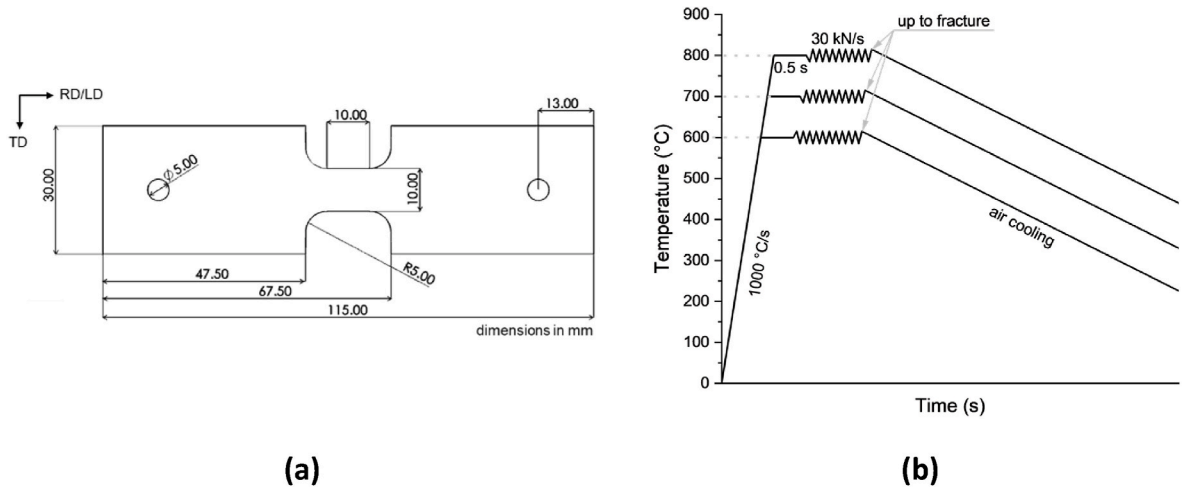

Fig. 2. Illustrations of (a) tensile specimens, indicating their dimensions and orientation and (b) Gleeble thermomechanical profile up to fracture. All dimensions are in mm. TD stands for transverse direction.

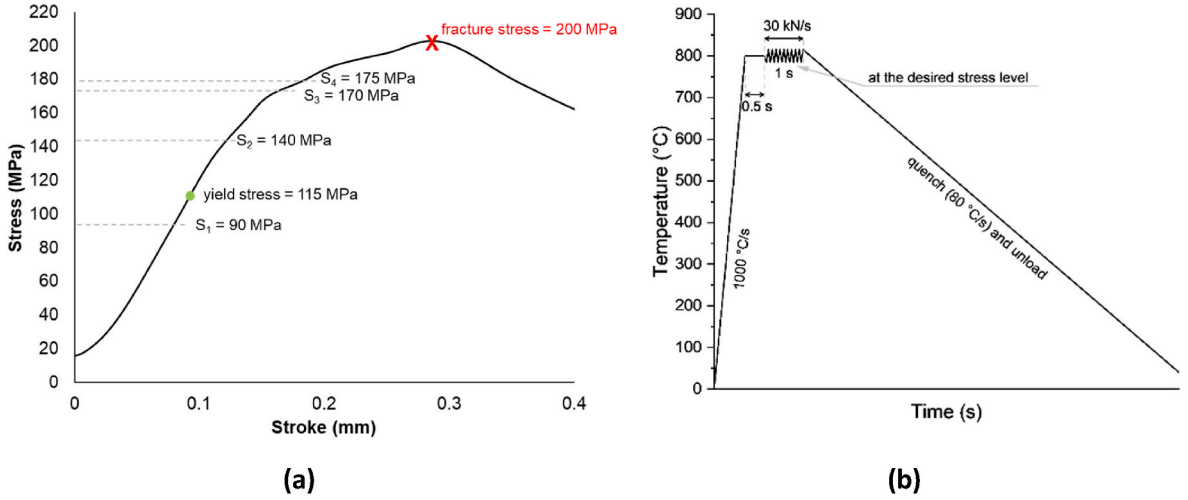

Fig. 3. Illustration of (a) stress-stroke curve of Zn-coated sample tested at 800 °C up to fracture indicating the selected stress levels – S1, S2, S3, and S4 – for the interrupted hot tensile and (b) theoretical thermomechanical interrupted test profile.

A high cooling rate was applied to suppress diffusional mechanisms and prevent further defect evolution, thereby retaining the chemical and defect configurations existing at 800 °C. The theoretical cooling curve is designed following a linear regression with a constant cooling rate of 78 °C/s, indicating a steady temperature decrease over time. However, the observed cooling behaviour has a non-linear temperature decrease that can be described by the polynomial regression $4.21x^2 - 165x + 1782.7$, where x represents time in seconds. While the overall cooling behaviour deviated from linearity, the average cooling rate within the temperature interval of 800 °C to 400 °C—encompassing the formation of Fe–Zn intermetallics and the temperature range where Zn remains in the liquid state—remained close to the intended 80 °C/s. Hence, the non-linear cooling does not significantly affect the interpretation of Zn diffusion or phase formation.

2.3. Characterisation of LME micromechanisms

To investigate LME micromechanisms, in-depth characterisation was performed on the cross-section of tensile specimens – rolling direction/loading direction (RD/LD) x normal direction (ND) plane – of interruptedly tested (S1, S2, S3, and S4) and fractured samples. Samples were metallographically prepared following grinding and polishing steps with 3 μm and 1 μm diamond paste and colloidal silica suspension (OPS). *Since the Zn coating and the TWIP steel vary in hardness and other characteristics, they behave differently during metallographic preparation. Therefore, following the previously described procedure, only the TWIP steel substrate will be adequately prepared for microscopic analysis. To study the Zn coating, the homogeneously heat-treated length of the tested specimen has been prepared in a JEOL SM-0910 cross-section polisher under an Ar + ion beam accelerating voltage of* 4 kV *and a current of* 12 μA *for 36 h. A silicon wafer has been glued on the sample's surface to protect the area of interest from beam damage.*

The *homogeneously tested volume in the TWIP steel substrate* cross-section of tensile specimens has been characterised using SEM, *EDS, electron backscattered diffraction (EBSD), and transmission electron microscopy (TEM). The EBSD data has been acquired on a Helios G4 PFIB SEM using a current of* 3.2 nA *for general scans and* 13 nA *for identification of intermetallics and an accelerating voltage of* 30 kV, *a tilt angle of 70°, and step size of* 50 nm *using TEAM-EDAX software in a hexagonal scan grid, and post-processing it with EDAX-OIM Analysis™ v8 software. The cleanup of EBSD data for the steel substrate has been the first post-processing step for some scans. First, neighbour orientation correlation with a grain tolerance angle of 15° and a cleanup level of 5 was applied for points with a confidence index lower than 0.1. Then, neighbour confidence index correlation cleanup*

was performed for points with a confidence index lower than 0.1. Afterwards, grains were defined with a tolerance angle of 15° and a minimum size of 5 pixels, with multiple rows required. For the Fe–Zn intermetallic layer, EBSD pattern quality was insufficient for successful indexing and phase discrimination using conventional Hough transform-based indexing [17]. For optimum indexing success, all patterns were recorded during EBSD data acquisition and processed off-line using NPAR [18] combined with the spherical indexing method available in the EDAX OIM Analysis 9 software. NPAR maximises the pattern quality and the spherical indexing method, then matches the optimised experimental EBSD patterns against dynamical or kinematical simulations [19]. As the entire pattern is used, the method is not dependent on detecting individual bands. The phase and orientation can be identified correctly for poor-quality patterns where only fragmented information is present. For this analysis, dynamical simulations [20] were prepared for the expected phases and the patterns in the EBSD maps were matched against all candidates. Indexing success is indicated by a cross-correlation coefficient that illustrates how well a pattern can be matched against the master pattern.

*The phase composition of the TWIP steel and the Zn-galvanised TWIP steel has been investigated before and after hot tensile tests by X-ray Diffraction (XRD) to study the phase transformations during the thermo-mechanical test. XRD experiments were performed using a Bruker D8 Advance diffractometer with Co-*Kα radiation. Diffractograms were recorded over the $15° \leq 2\,\theta \leq 60°$ range, with a step size of 0.028° in 2θ and counting time per step of 1s for investigating the coating through its entire thickness and the steel substrate. The penetration depth of XRD in Zn was calculated in the AbsorbDX (Bruker) as approximately 13 μm and 28 μm for 2 θ of 40° and 100°, respectively. This was done to verify whether the full Zn coating thickness would be able to be analysed. CALPHAD thermodynamic simulations via ThermoCalc were also performed for the steel composition under study to understand which Fe–Mn–Zn phases are likely to form under equilibrium conditions. Note that only Fe-based phases and Fe–Zn intermetallics were selected in the database to be represented, and the chosen temperature was 400 °C, which is the lowest temperature thermodynamically simulated results are experimentally verified by ThermoCalc. *To analyse more accurately the Zn diffusion into the steel substrate, Electron Probe Micro Analysis (EPMA) was performed with a JEOL JXA 8900R microprobe, using an electron beam energy of* 10 keV *and beam current of* 50 nA *employing Wavelength Dispersive Spectrometry (WDS). To locally investigate the LME micromechanisms involved in the early-stage cracking, cross-sectional TEM samples were produced from the surface of the S4 condition by focused ion milling (FIB) in a Helios G4 PFIB SEM. This lamella has been analysed by a* FEI cubed Cs corrected Titan and elemental mapping was done in STEM, using the super-X in the ChemiSTEM™ configuration. Transmission Kikuchi diffraction (TKD) has been performed in the TEM lamella in the *Helios G4 PFIB SEM using* 13 nA *and* 30 kV *at a – 30° tilt angle.*

3. Results

3.1. Fe–Zn interactions

Studying the Zn–Fe interactions is key to understanding LME micromechanisms. Fig. 4 displays representative cross-sectional SEM micrographs and EDS elemental maps for Fe and Zn of interruptedly tested tensile specimens at S1, S2, S3, and S4 stress levels, at 800 °C, where x is the distance from the control thermocouple (specimen's centre). By integrating data from SEM and EDS, the following points were observed: (1) after the hot tensile tests, the steel substrate exhibits defects including microcracks and surface-connected cavities with variable severity of damage, where slightly and strongly affected zones alternate, irrespective of the distance from the control thermocouple; (2) with temperature and stress, Zn is seen to have diffused across the steel substrate within a contained area; (3) the depth of the diffused Zn layer in the steel substrate varies according to the damage severity and the

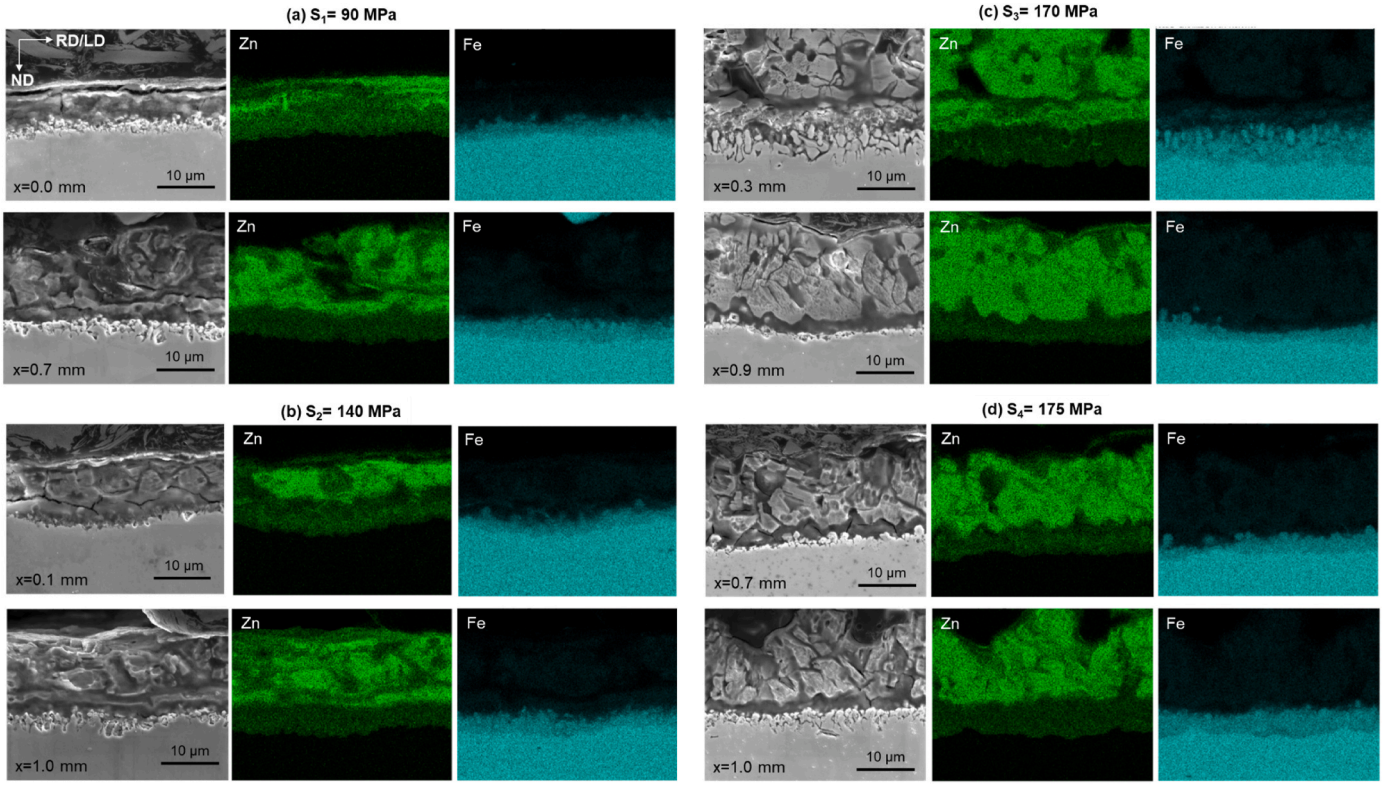

Fig. 4. SEM micrographs in secondary electrons (SE) mode of the cross-section surfaces of tensile specimens tested at 800 °C and (a) S1 = 90 MPa, (b) S2 = 140 MPa, (c) S3 = 170 MPa, and (d) S4 = 175 MPa conditions and their respective Zn and Fe EDS maps. x is the distance between the analysed area and the control thermocouple position.

applied stress level; and (4) during hot tensile tests, the Zn coating undergoes transformation due to diffusion reactions between Zn and Fe. These observations will be further examined in the following paragraphs. For points 1 and 3, the defect density is beyond the scope of the current study, which focused on the comparative microstructural analysis between damaged and non-damaged areas.

The Zn and Fe EDS maps show that, in all stress levels, Zn diffuses across the steel substrate, forming a Zn-rich austenite layer (γ-Fe(Zn)) with a wavy-shape front (Fig. 4). Fig. 5 (b) and 5 (c) show the EPMA elemental distribution maps of Zn and Al, respectively, measured over the area highlighted in Fig. 5 (a). The colour bars represent the relative concentration levels. The quantitative line scan results for Zn, Al, and Fe along the line indicated in Fig. 5 (a) are displayed in Fig. 5 (d). The higher sensitivity of EPMA compared to EDS reveals that the Zn concentration within the γ-Fe(Zn) layer is not uniform. Instead, it exhibits a gradient, decreasing progressively as it extends deeper into the steel substrate. Note that the EPMA maps also show that after tensile testing at 800 °C, the Al signal at the interface appears as discrete regions of varying intensity along the interface, indicating a discontinuous distribution in the interface (pointed out by the white arrows in (Fig. 5 (c)), in contrast to the continuous layer observed in the as-received material (Fig. 1).

The depth of Zn diffusion into the steel substrate varies depending on the severity of damage and the applied stress level (Fig. 6). About 20 to 40 Zn depth measurements were made for non-damaged and damaged conditions, respectively, for each investigated stress level (S1 – S4). Statistical analysis using ANOVA followed by Tukey's HSD post-hoc test was performed to assess statistical differences. In this context, stress conditions with ***p*-values lower than 0.05** were considered statistically different, indicating a low probability that the observed difference occurred by chance.

Across the damaged areas, Zn diffusion depths under stress

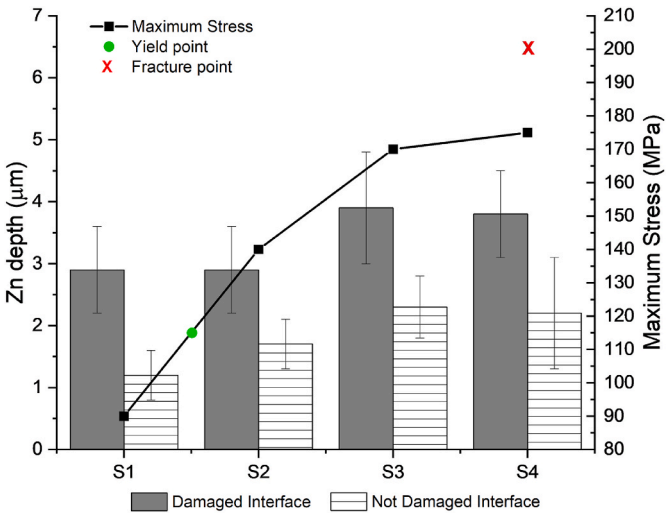

Fig. 6. Zn signal depth into the steel substrate as a function of the stress level and the appearance of the steel substrate, damaged or not damaged.

conditions **S1** and **S2**, where the applied stress is below or near the yield strength, were comparable, averaging around **3 μm**. Under **S3** and **S4**, where the applied stress exceeded the yield strength by a larger margin, Zn depths were comparable, at approximately 4 **μm,** and greater than S1 and S2. Statistical differences between all stress conditions were significant **except between S3 and S4 (*p*-value higher than 0.05),** likely due to the relatively small stress increment of **5 MPa** between them.

In the **non-damaged regions**, Zn diffusion depths were considerably lower overall, increasing slightly with stress up to S3. As in damaged areas, S3 and S4 stress levels presented similar average values (2.3 and

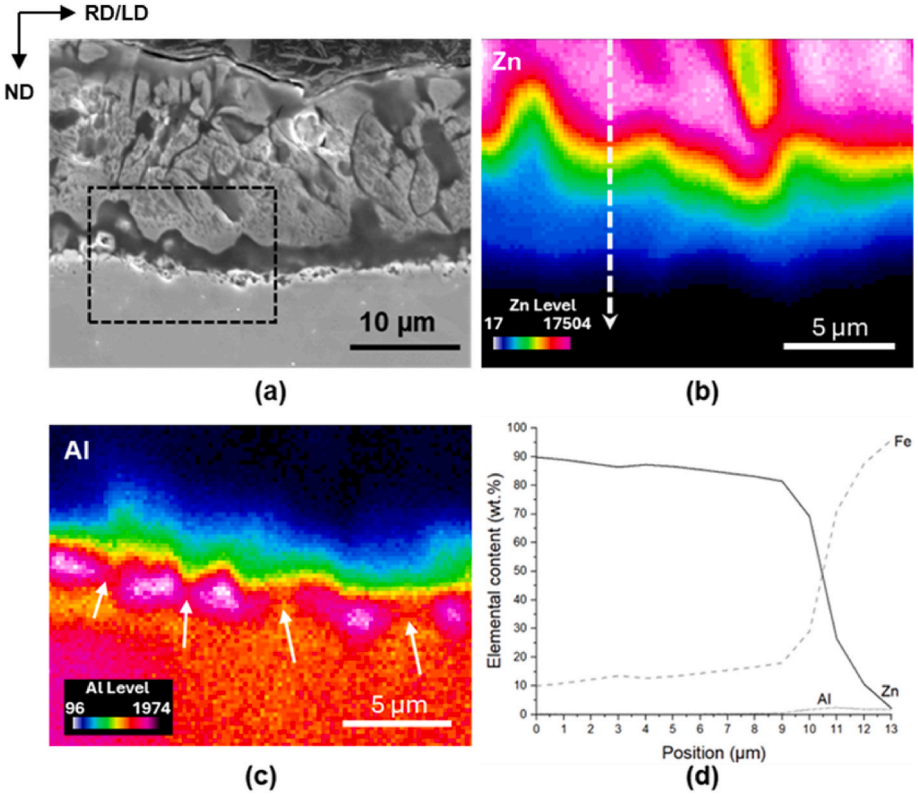

Fig. 5. (a) SEM micrograph of a cross-section area of the tensile specimen interruptedly tested at S3 = 170 MPa and 800 °C and EPMA (b) Zn map, (c) Al map and (d) linescan profile of Fe, Zn, and Al of the area within the dashed rectangle in (a) and dashed line in (b). The white arrow in (b) represent the EDS scanning line. The white arrows on (c) point out to discontinuous parts of Al layer on the interface.

2.2 **µm, respectively)**, and statistical differences between all stress conditions were also significant, **except again between S3 and S4**. Lastly, the large standard deviation bars in Fig. 6 reflect substantial local variation in Zn diffusion, likely driven by **microstructural heterogeneities**.

For all the discussed cases, the diffusion is considered considerable for a thermomechanical process of 1.5 s at 800 °C, which suggests a rapid diffusion process beyond expected equilibrium predictions. Concerning the shape of the diffusion front, the correlative microscopy, which combines high-magnification EBSD and EDS (Fig. A2 in Appendix A), reveals that the wavy shape is attributed to grain boundaries mostly with misorientation angles in the range of 40°–54°. Interestingly, it can also be seen in Fig. 4 that defects on the steel substrate are contained within the boundaries of γ-Fe(Zn) layer.

3.2. Characterisation of Fe–Zn intermetallics

Transformations within the Zn coating occur during hot tensile testing due to Zn–Fe diffusion reactions (Fig. 4). These transformations are evident from changes in both the coating's appearance and the distribution of Zn and Fe compared to the as-received condition (Fig. 1). To assist in analysing phase transformations in this system, a ternary Fe–Mn–Zn phase diagram was simulated using Thermo-Calc (Fig. A1 in Appendix A). However, the LME process is inherently non-equilibrium in nature, involving rapid heating and short exposure times that deviate significantly from equilibrium thermodynamic conditions. This may lead to potential discrepancies between theoretical and actual phase compositions. Therefore, experimental verification was conducted using XRD, EDS, and EBSD to confirm the phases present after Gleeble hot tensile tests.

XRD analysis reveals that the as-received (AR) material consists of Zn, ZnO, and γ-Fe, corresponding to the coating and steel substrate, respectively (Fig. 7(a)). In contrast, interruptedly tested specimens (S1, S2, S3, and S4) contain Fe–Zn intermetallic phases, including $FeZn_{10}$ (δ), Fe_3Zn_{10} (Γ), and Fe_5Zn_{21} (Γ1), as shown in Fig. 7(a). Due to their similar cubic crystal structures, Γ and Γ1 are difficult to distinguish via XRD and are therefore collectively represented as Γ [21]. Notably, the XRD spectra for all interruptedly tested specimens are nearly identical, indicating that tensile stress does not influence the formation of Fe–Zn intermetallics.

A combined EDS and EBSD analysis was conducted to examine the distribution of Fe–Zn intermetallic phases—ξ, δ, Γ, and Γ1—within the

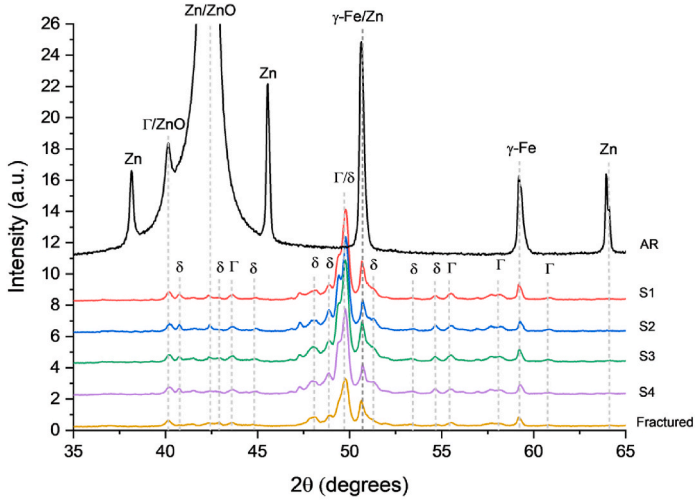

(a)

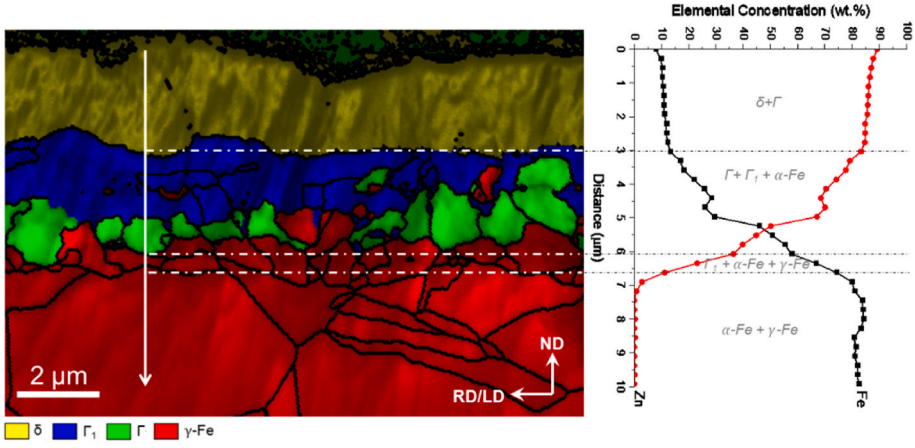

(b)

Fig. 7. (a) XRD spectra of the RD x TD plane of the as-received (AR) Zn-galvanised TWIP steel, the hot tensile specimens tested up to fracture and interruptedly tested at S1, S2, S3, and S4 stress conditions at 800 °C, and (b) EBSD phase maps of the interruptedly tested S1 = 90 MPa specimen includes the EDS line scan elemental analysis where the thermodynamically simulated phases are represented in the elemental concentration-distance plot. The white arrow in b) represent the EDS scanning line.

coating. Fig. 7(b) presents the spherical indexing cross-correlation map overlaid with the phase map, alongside the Fe and Zn elemental distribution along the EDS linescan. Based on the measured Fe and Zn contents, the thermodynamically predicted phases are indicated in grey within the corresponding regions in the chart.

Additionally, grains near the steel substrate were successfully indexed with a body-centred cubic (BCC) crystal structure. However, ferrite was ruled out as a possibility, as it was not detected in the XRD analysis. Furthermore, Fe and Zn content in this layer suggested it was most likely a cubic Γ phase. Although Zn stabilises ferrite, the high Mn content in TWIP steel, known as an austenite stabiliser, prevents ferrite formation near the substrate. It is also worth noting that, while the intermetallic phases in Fig. 7(b) appear in well-defined layers, in other regions, their distribution was more irregular (see Fig. A3 in Appendix A). Overall, the experimental results correlate well with thermodynamically predicted equilibrium phases.

3.3. LME damage micromechanisms

Having analysed Fe–Zn interactions during the early stages of LME, the focus shifts to understanding the micromechanisms of LME damage. Examination of damaged regions in the cross-section of tensile specimens near failure (S3 condition) reveals a stronger Zn signal within the wider damaged areas of the steel substrate, as highlighted by the dashed white rectangles in Fig. 8(a). This observation suggests that liquid Zn has percolated through the cracks. Additionally, EDS and EPMA analyses at this scale (Figs. 4, 5 and 8) show no evidence of preferential Zn diffusion along grain boundaries.

Crystallographic analysis of the damaged areas under the S3 condition provides further insight into LME micromechanisms in its early stages. A comparison between the SEM micrograph and the IPF map indicates that many regions appearing as part of the steel substrate (well-polished areas indicated by black arrows in Fig. 8(a)) are not indexed as austenite (Fig. 8(b)), despite displaying high-quality diffraction patterns. This characteristic has been similarly observed for intermetallic phases, reinforcing the hypothesis that liquid Zn percolates through the γ-Fe(Zn) layer at high temperatures. The IPF map analysis (Fig. 8(b)) further reveals that at least 20 % of the austenitic grains within the damaged γ-Fe(Zn) layer exhibit clear signs of transgranular damage. This fraction may be underestimated as, in some areas, the separation between grains is significant, making it difficult to distinguish between transgranular and intergranular defect patterns. Moreover, certain grains also display atypical shapes, with irregular and disrupted morphology, with internal void-like regions (e.g., pink grain in Fig. 8(b) on the upper left side), and distorted jagged boundaries where they interface with adjacent grains (e.g., light-blue grain in Fig. 8 (b) on the upper central area). This may also indicate transgranular degradation. However, confirming this interpretation is challenging in the absence of an adjacent grain section with the same orientation.

TEM analysis was conducted on a FIB-milled lamella from the S4 condition (Fig. 9). The results reveal that defects caused by the interaction of liquid Zn with the steel substrate terminate at steel grain boundaries. Furthermore, EDS linescans across grain boundaries—both those connected to and isolated from damaged regions (Fig. 9(b) and (c), respectively)—provide insight into Zn diffusion behaviour at the nanoscale. Zn diffusion was detected along grain boundaries connected to damaged areas, with Zn concentrations ranging between 4 % and 10 % within regions extending 5 nm–45 nm in length. Considering the grain boundary thickness of approximately 0.5 nm [22], it indicates that lateral bulk Zn diffusion into neighbouring grains occurred. In contrast, no Zn diffusion was observed in isolated grain boundaries.

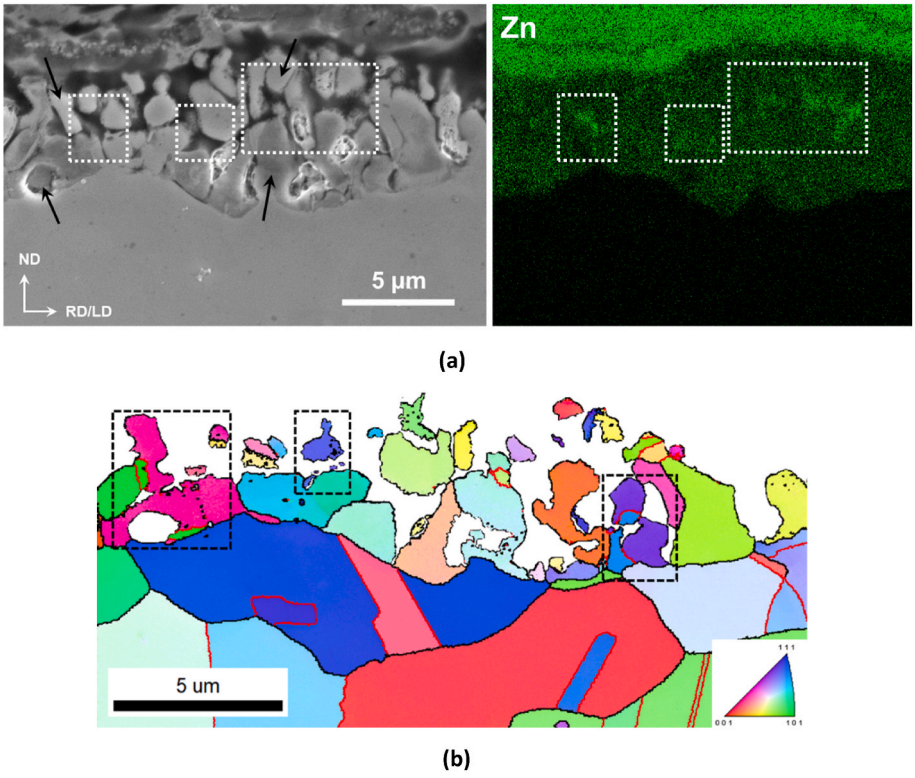

Fig. 8. (a) SEM micrograph and Zn EDS elemental map and (b) IPF-ND-section surface of a tensile specimen interruptedly tested at S3 = 170 MPa and 800 °C. The dashed rectangle in (a) and (b) highlight the areas with higher concentrations of Zn and areas of transgranular fracture, respectively. Black arrows in (a) indicate well-polished areas that are not indexed as austenite, despite their good diffraction patterns, likely indicating the presence of Fe–Zn intermetallics. Black and red lines in (b) are high-angle and ∑3 grain boundaries, respectively.

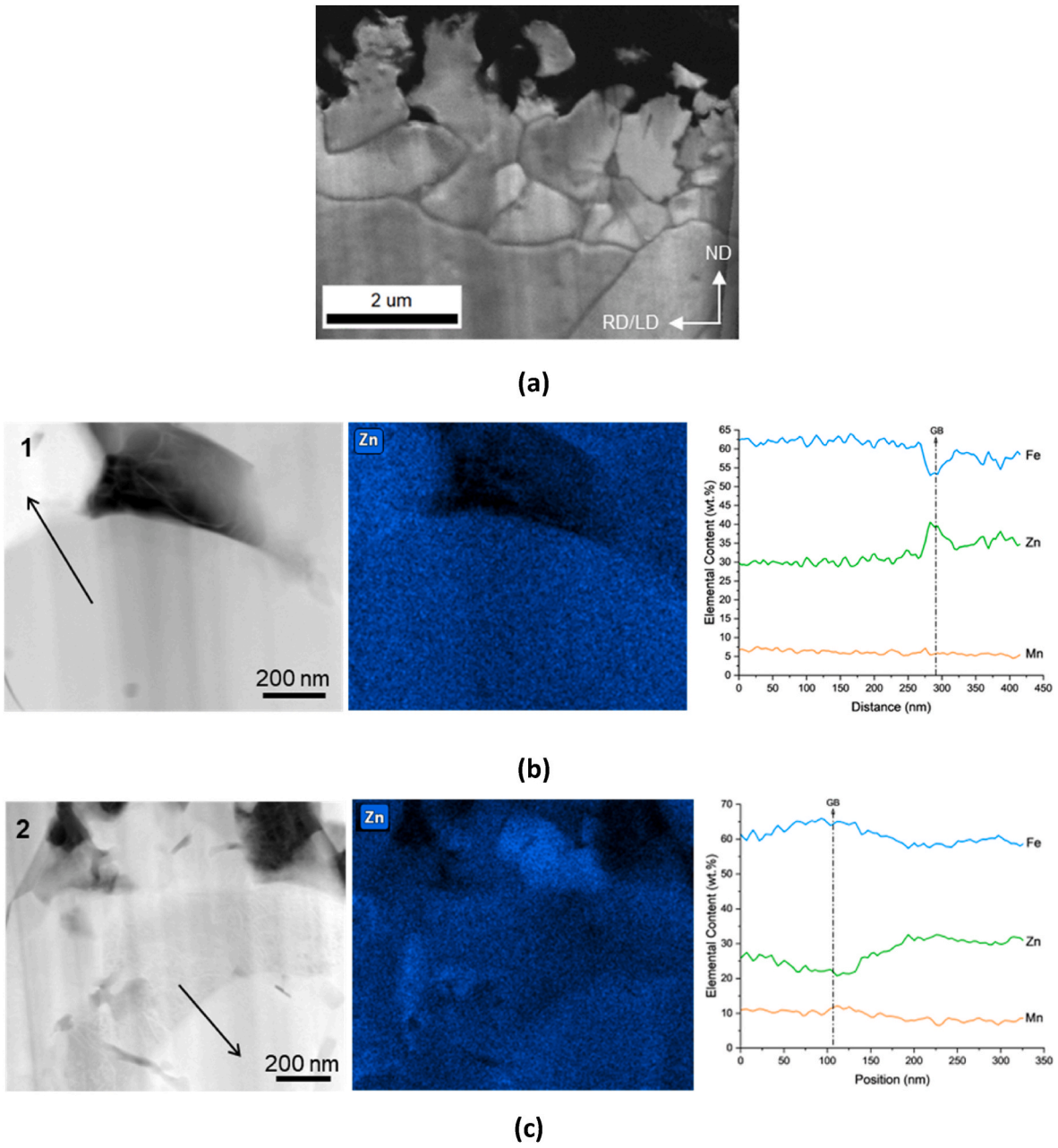

Fig. 9. TKD, TEM, and EDS analysis of a FIB-milled lamella from S4 = 175 MPa. (a) Image quality map showing the position of grain boundaries relative to defects generated by Fe dissolution in liquid Zn. (b) and (c) TEM micrograph, Zn EDS map, and elemental content-position plot of Fe, Zn, and Mn measured along a grain boundary linked and not linked to defects, respectively. The black arrows in (b) and (c) represent the EDS scanning line.

4. Discussion

4.1. Zn diffusion in Fe

The as-received Zn-galvanised TWIP steel has a thin, continuous Fe–Al inhibition layer (Fig. 1). This layer is formed during galvanisation by the strong affinity between Al – present in the Zn coating – and Fe – from the steel substrate. Its presence prevents Fe–Zn reactions, and, consequently, the formation of Fe–Zn intermetallics [13,23]. However, the Fe–Al inhibition layer is known to break down at elevated temperatures (between 420 °C and 800 °C) [13,24–26]. Consequently, Fe–Zn interdiffusion and severe reaction between liquid Zn and the steel substrate occur, as shown in Figs. 4 and 5.

The Zn diffusion into the steel substrate is substantial, asymmetrical, and exhibits a wavy front. These observations suggest that Zn transport in Fe does not follow a conventional lattice diffusion mechanism but occurs through an alternative transport process. Based on the reported lattice diffusion coefficient in austenite, $D^{\gamma}_{Zn} = 1.13\text{x}10^{-14}$ m^2 s^{-1} at 900 °C [27], the diffusion coefficient at 800 °C was estimated using an activation energy range of 218–263 kJ/mol and a pre-exponential factor between $2\text{x}10^{-4}$ to $6\text{x}10^{-3}$ m^2 s^{-1} for Fe diffusion in Zn [28]. Due to the absence of direct experimental data for Zn diffusion in γ-Fe, these Fe-in-Zn parameters were used as an approximation. The calculated diffusion coefficient for Zn in γ-Fe at 800 °C lies between $9.5\text{x}10^{-16}$ and $4.9\text{x}10^{-15}$ m^2 s^{-1}. Thus, the expected diffusion depth after 1.5 s (total time at 800 °C during the hot tensile test) corresponds to approximately 50–130 nm. Note that the diffusion of Fe in Zn is expected to be faster than the diffusion of Zn in Fe. Since at 800 °C Zn is in a liquid state, it allows for significantly higher atomic mobility and faster diffusion. Consequently, the calculated diffusion coefficients and the diffusion

depths for Zn in Fe of 50–130 nm are likely overestimated. Still, the measured Zn diffusion depth in our experiments is approximately 3 μm, about two orders of magnitude greater than the predicted values. One factor that should be considered in the diffusion process is stress. Notably, under stresses well above the yield point, as in the S3 and S4 conditions, the Zn diffusion depth increases, indicating a stress-assisted process. However, it is observed that the increase in the applied stress from 90 MPa (S_1, below yield stress) to 175 MPa (S_4, well above yield stress) results in about 35 % increase in Zn diffusion depth. However, attributing such an extensive Zn penetration (3–4 μm instead of 50–130 nm) solely to stress-assisted lattice diffusion would require an unrealistically high diffusion coefficient. Shewmon, Abbas, and Meyrick [29] observed similar diffusional behaviour in their study of a Fe–Zn couple after annealing. Note that their experiments were performed under significantly different thermal and temporal conditions compared to those representative of LME during welding. Specifically, their annealing treatments were performed at 450 °C for durations ranging from 12 to 192 h, and at 550 °C for durations between 3 and 192 h. Despite these differences, they reported unexpectedly rapid diffusion rates for their annealing conditions, a finding comparable to the accelerated diffusion observed in our study under LME conditions. The authors reported three relevant aspects for this study: 1) the abnormally fast diffusion in a Fe–Zn couple of 2–4 orders of magnitude higher than in lattice diffusion; 2) the inhomogeneous diffusion where interfaces had both negligible and considerable diffusion within the same sample; and 3) discontinuous changes in Zn concentration from consecutive grains at the same distance from the steel surface (as observed in this study due to the wavy diffusional front (Fig. 8(b)) [29]. behaviour to diffusion-induced grain boundary migration (DIGM) [29]. DIGM occurs when solute atoms diffuse along grain boundaries, such as Zn in the steel substrate, and some of them diffuse into adjacent grains, generating a chemical gradient. Consequently, this gradient acts as a driving force for grain boundary movement, leaving behind an enriched zone of diffusing atoms. In this study, the presence of a chemical gradient is supported by TEM observations (Fig. 9), which revealed Zn diffusion along grain boundaries adjacent to damaged areas and lateral bulk Zn diffusion into adjacent grains. This phenomenon results in accelerated solute transport under conditions where lattice diffusion would be negligible [30]. Notably, the measured diffusion depth is approximately two orders of magnitude higher than expected for bulk diffusion of Zn in γ-Fe at the same temperature and holding time. Based on the relationship $x = \sqrt{Dt}$, where x is the diffusion depth, D the diffusion coefficient, and t the diffusion time, this suggests an effective diffusion coefficient about four orders of magnitude higher than the usual bulk diffusivity, further supporting the involvement of fast diffusion pathways such as DIGM. As diffusion is led by boundary migration, DIGM results in a wavy diffusion front which follows the boundary shape, as observed in this study (Figs. 4, 5 and 8). Moreover, the grain boundary migration may significantly vary from boundary to boundary [30–32]. For instance, coherent twin boundaries such as $\sum 3$ are not observed to undergo DIGM [30,32].

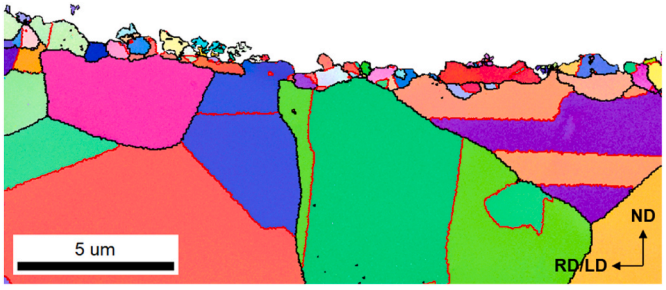

Fig. 10. IPF-ND of a non-damaged cross-section surface of a tensile specimen interruptedly tested at S3 = 170 MPa and 800 °C. Black and red lines are high-angle and $\sum 3$ grain boundaries, respectively.

By comparing IPF maps from damaged (with higher Zn diffusion depth, Fig. 8) and non-damaged areas (with lower diffusion depth, Fig. 10) of an S3 sample, it was observed that the percentage of Σ3 grain boundaries in the first layer of grains adjacent to the Zn coating was higher in non-damaged regions (45 %) compared to damaged regions, in grains where bulk Zn diffusion had occurred (25 %). Special grain boundaries, especially $\sum 3$ ones, have the highest symmetry and, consequently, lower free volume, mostly acting as diffusion barriers [33–36]. In this case, since the defects on the steel substrate were observed to be limited to the γ-Fe(Zn) layer, the lower severity of damage in certain areas may be attributed to the lower diffusion paths leading to less driving force for grain boundary migration. This correlation between $\sum 3$ grain boundaries and the reduced solid-state Zn bulk diffusion is observational and needs to be confirmed.

To support the hypothesis of DIGM in the investigated material, the size of grains at the interface in the as-received and damaged zones was measured and found to be comparable at 2.5 μm. However, the grain size in the affected areas by the liquid Zn is very likely underestimated due to the considerable severity of damage. Hence, it is difficult to confirm the DIGM event. Thus, while DIGM is proposed as a plausible mechanism, further *in situ* or time-resolved studies are needed to confirm its occurrence.

Concurrently with the atomic diffusion of Zn into Fe, liquid Zn severely reacts with the steel substrate, assisting the Fe diffusion into liquid Zn.

4.2. LME damage and micromechanisms

Although intergranular cracking is typically a key characteristic of LME micromechanisms [9–12], it was observed that the initial exposure to liquid Zn led to transgranular deterioration in at least 20 % of the austenitic grains of the steel substrate. This suggests that different micromechanisms may be active at the onset of the LME process. This behaviour aligns with the well-established aggressive corrosive nature of liquid Zn, which has been shown to dissolve Fe in Zn-galvanised steels [37–39]. Peng, Wu, and Zhang [37] performed *in situ* high-temperature confocal laser scanning microscopy analysis and observed the erosion-corrosion effect of liquid Zn in a 22MnB5 steel. Their study showed surface defects similar to those observed in this work (Fig. 4). Hence, the observed transgranular cracking may be attributed to the dissolution-driven degradation of the steel substrate caused by liquid Zn.

However, in Ref. [37], the first sign of erosion-corrosion appears at 510 °C, with a heating rate of 8 °C/s. This means that the heating process from room temperature to 510 °C took about 60 s, which is significantly longer than the 1.5 s holding time at 800 °C used in Gleeble simulations herein. Nevertheless, it is important to consider that the erosion-corrosion rate increases sharply with the liquid Zn temperature [40]. To evaluate the plausibility of this mechanism under our shorter timescales, we refer to the findings of Wang et al. [40], who observed that increasing the temperature of liquid Zn from 520 °C to 550 °C raises the erosion-corrosion rate in 316L austenitic stainless steel from 120 to 230 μm h^{-1}. Based on their data between 460 °C and 550 °C, we performed an exponential regression ($y = 0.0256e^{0.0164x}$) to extrapolate the erosion-corrosion rate to 800 °C. The resulting projected rate at 800 °C is approximately 12770 μm h^{-1}. At this rate, during the 1.5s holding at 800 °C in the Gleeble hot tensile tests performed in this study, the expected dissolution depth is around 5 μm. This supports the hypothesis that erosion-corrosion can realistically occur within the Gleeble simulation of RSW timeframe and may contribute to the early stages of LME cracking. As a result of this dissolution, Fe from the steel substrate diffuses into the molten Zn coating [38,41,42]. In this scenario, defects generated at the interface create additional surface area, which can improve the wetting behaviour of liquid Zn on steel. Moreover, the presence of these defects intensifies the local stress field at grain boundaries (crack tips coinciding with austenitic grain boundaries (Fig. 9(a)), likely enhancing Zn grain boundary diffusion and

accelerating the LME process, increasing its severity [43]. From here, three mechanisms may act to induce grain boundary decohesion and initiate LME cracking according to the literature: 1) pure solid-state Zn atomic diffusion [9,10]; 2) formation of liquid Zn when Zn reaches its solubility in γ-Fe [14]; and 3) formation of Fe/Zn intermetallics leading to local heterogeneous stress distribution [44]. The first hypothesis is based on the Klinger-Gordon-An grain boundary diffusion model [9,10]. In this case, the solid-state Zn grain boundary diffusion leads to grain boundary decohesion and cracking. The second theory is similar, but considering that when Zn atoms at grain boundaries reach their solubility in austenite, they form liquid Zn [14]. This liquid Zn film weakens the metallic bonds by adsorption-induced decohesion [15], opening a new crack. Lastly, the third premise is based on recent studies that observed the nucleation of Fe–Zn intermetallics along grain boundaries at high temperature, which results in local stress, favouring cracking [44]. To assess the plausibility of intermetallic formation at 800 °C at grain boundaries, we considered the local compositions measured via TEM-EDS (Fig. 9(b): 53 wt% Fe, 39 wt% Zn, 8 wt% Mn) along grain boundaries ahead of defect tips. According to the Fe–Zn–Mn ternary equilibrium diagram at 800 °C (Fig. A4, Appendix A), the presence of the Γ phase (Fe_3Zn_7) at grain boundaries is possible. However, no conclusion can be drawn from this information since the experimental conditions — notably the very rapid heating rate (1000 °C/s) and brief holding time (1.5 s at 800 °C) — deviate significantly from equilibrium, limiting the applicability of equilibrium phase predictions via Thermo-Calc. Once the crack is formed, fresh liquid Zn percolates the crack, providing a readily available source of Zn atoms to diffuse through the grain boundaries and continue the LME process up to fracture.

During cooling to room temperature, the liquid Zn enriched in Fe transforms into Fe–Zn intermetallics such as $FeZn_{10}$ (δ), Fe_3Zn_{10} (Γ), and Fe_5Zn_{21}(Γ_1), as observed in Fig. 7. The presence of intermetallics inside the crack of a specimen tested up to fracture (Fig. A5, Appendix A) confirms the percolation of liquid Zn in the steel substrate at high temperatures. However, it is important to mention that some of these intermetallics may also have formed at 800 °C as previously explained.

To provide a visual overview of the mechanisms discussed above, Fig. 11 schematically describes the early-stage cracking LME micromechanisms. It highlights the Fe–Zn interactions and mechanisms of Zn diffusion and grain boundary weakening that promote embrittlement. The LME stages compatible with our experimental observations are.

1. Upon heating from room temperature to 800 °C, the continuous Fe–Al inhibition layer observed at as-received Zn-galvanised TWIP steel (Fig. 1), which separates the steel substrate from the Zn coating, locally breaks down (Fig. 5). This degradation exposes the austenitic steel substrate to direct contact with liquid Zn, enabling the onset of interfacial reactions and diffusion processes. This step is crucial in initiating the conditions necessary for subsequent Fe–Zn interactions.
2. Once the steel substrate is exposed to liquid Zn, Zn atoms very likely begin diffusing along high-diffusivity paths, i.e., grain boundaries. Observed features such as uneven Zn diffusion — with areas of both limited and extensive diffusion within the same sample — and a wavy diffusion front (Fig. 4) suggest that this process is probably enhanced by diffusion-induced grain boundary migration (DIGM). At the same time, defects appear on the steel surface (Fig. 4) and may be attributed to localised dissolution of the steel substrate through erosion–corrosion as liquid Zn aggressively interacts with the steel surface. This dissolution also promotes outward Fe diffusion into the liquid Zn.
3. Defects generated on the steel surface during the dissolution stage by liquid Zn act as preferential pathways for liquid Zn percolation. These defect tips, which predominantly coincide with grain boundaries (Fig. 9), amplify local stress concentrations at these interfaces. The combined effect of localised stresses and the accumulation of liquid Zn at these sites enhances Zn atomic diffusion along the grain boundaries. As a result, grain boundaries adjacent to these defect tips become progressively enriched with Zn (Fig. 9), accelerating the conditions for embrittlement.
4. At this point, three mechanisms are possible for causing grain boundary decohesion and LME cracking: 1) pure solid-state Zn atomic diffusion; 2) solid-state Zn atomic diffusion followed by the formation of a liquid Zn film when Zn reaches its solubility in γ-Fe; and 3) formation of Fe–Zn intermetallics leading to local heterogeneous stress distribution.
5. Following crack initiation, liquid Zn infiltrates the newly formed intergranular cracks, effectively replenishing the crack path with embrittling liquid Zn. This percolation process maintains further Zn atom accumulation at grain boundaries ahead of the crack tip. Consequently, the local conditions for intergranular weakening are re-established, perpetuating a cyclic embrittlement mechanism wherein stages from (3) repeat, driving progressive crack propagation under sustained mechanical and thermal conditions.

One of the most widely accepted LME models [9,10], along with many related studies [3,14,15] in Zn-galvanised TWIP steels, describes LME solely as a diffusion-driven phenomenon. While this framework captures important aspects of LME behaviour, our findings suggest a synergistic role of DIGM and dissolution of the steel substrate by liquid Zn by erosion-corrosion active in the early stages of embrittlement. These insights provide a more comprehensive understanding of LME and can support the development of targeted mitigation strategies and optimised material design. Such advancements are essential for enhancing the performance and reliability of Zn-coated steels submitted to high-temperature and stress processes (e.g., resistance spot welding and forming), particularly in automotive applications.

5. Conclusions

This study successfully identified the early-stage liquid metal embrittlement (LME) cracking mechanisms in Zn-galvanised, fully-austenitic, twinning-induced plasticity (TWIP) steel through interrupted Gleeble hot tensile tests and comprehensive microscopic analyses. In this investigation, the degradation sequence and the contributing factors that control the onset of LME were established. The key findings are as follows.

1. The onset of LME appears to be associated with a synergistic role of diffusion-induced grain boundary migration and the dissolution of the steel substrate by liquid Zn through erosion-corrosion. Fast solid-state bulk Zn diffusion is observed to form a γ-Fe(Zn) layer, within which dissolution defects are confined.
2. Defects formed on the steel surface in contact with liquid Zn are observed to be heterogeneous, resulting in damaged and non-damaged areas within the same sample. The character of the austenitic grain boundaries at the steel surface likely governs the severity of surface degradation. Non-damaged areas show a higher fraction of $\sum 3$ boundaries (45 %) than damaged areas (25 %), whose high symmetry is known to hinder grain boundary diffusion and suppresses DIGM. As a result, $\sum 3$ grain boundaries likely limit the steel surface deterioration.
3. Following the initial surface degradation stage, experimental observations indicate grain boundary diffusion ahead of defect tips, which preferentially align with austenitic grain boundaries. Local stress amplification at these defect tips likely enhances Zn grain boundary diffusion and may accelerate the LME process. Consequently, these sites facilitate a more rapid Zn accumulation along neighbouring grain boundaries compared to regions without such defects, intensifying embrittlement conditions.
4. The accumulation of Zn atoms along grain boundaries may lead to grain boundary weakening and, under tensile stress, promote

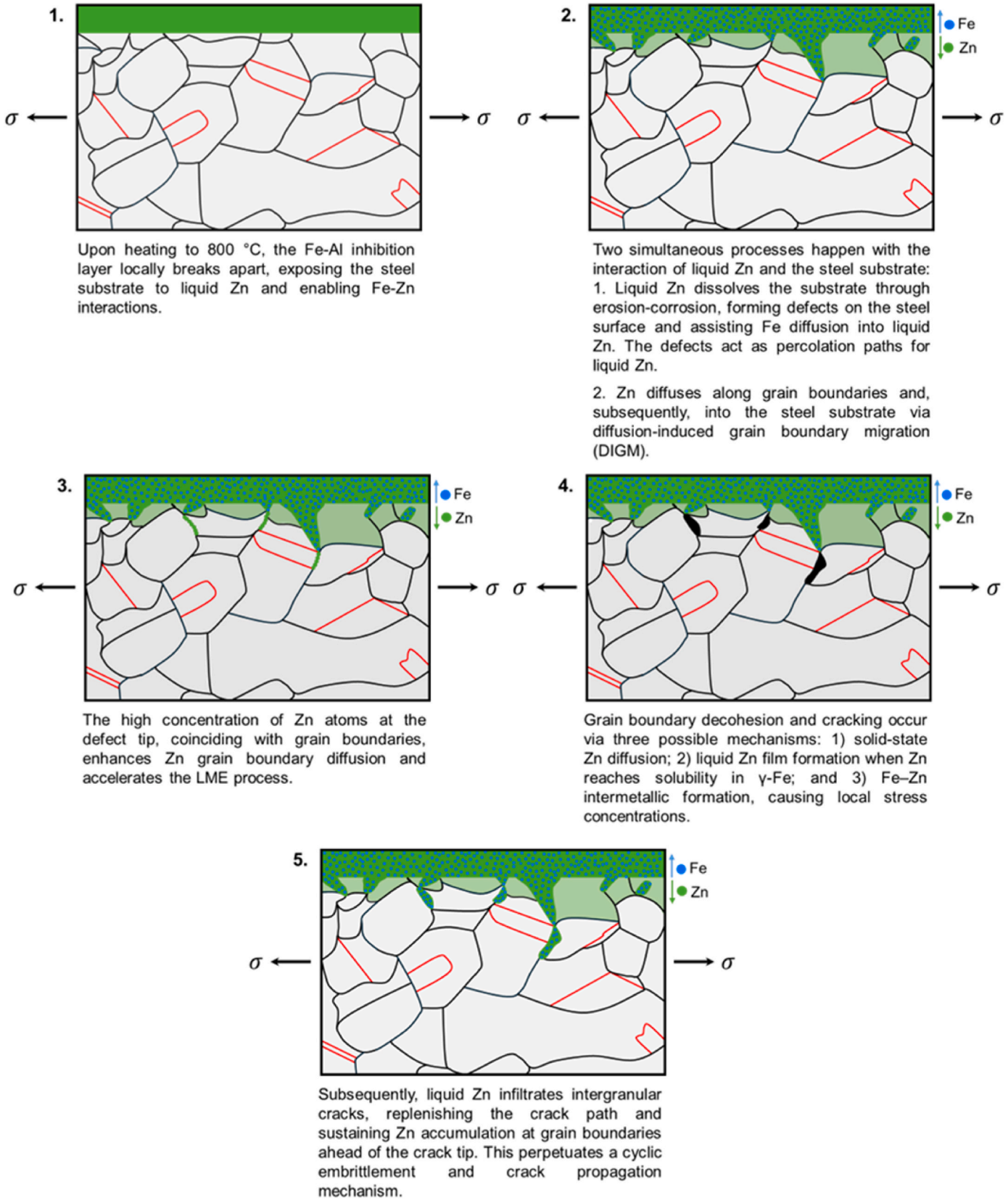

Fig. 11. Schematic illustration of the sequential steps leading to the onset of LME in the studied Zn-galvanised TWIP steel. The black and red lines represent high-angle random and ∑3 CSL grain boundaries, respectively. σ is the tensile residual stress.

cracking through three possible mechanisms: (1) pure solid-state Zn diffusion; (2) liquid Zn film formation once Zn reaches its solubility limit in γ-Fe; and (3) Fe–Zn intermetallic formation, generating local stress concentrations.

5. Once the cracks form, they become infiltrated by liquid Zn, supplying new Zn atoms to the forward grain boundaries. Then, the local conditions for solid-state Zn grain boundary diffusion and intergranular weakening are re-established, sustaining crack growth until fracture occurs.

This study provides a foundational understanding of the micromechanisms governing early-stage LME cracking in Zn-coated TWIP steels. Future research will focus on how microstructure influences crack propagation, particularly the role of grain boundaries and their orientation to applied stress. Establishing these relationships will offer deeper insights into factors controlling crack growth and resistance, contributing to the design of LME-resistant steels.

CRediT authorship contribution statement

Virgínia Bertolo: Conceptualization, Methodology, Validation, Formal analysis, Investigation, Resources, Data curation, Writing – original draft, Writing – review & editing. **Gautham Mahadevan:** Conceptualization, Writing – review & editing. **René de Kloe:** Methodology, Validation, Writing – original draft, Writing – review & editing. **Roumen H. Petrov:** Conceptualization, Validation, Writing – review & editing, Supervision. **Vera Popovich:** Conceptualization, Validation, Writing – review & editing, Supervision, Project administration.

Data availability statement

The raw/processed data required to reproduce these findings cannot be shared at this time as the data also forms part of an ongoing study.

Declaration of competing interest

The authors declare that they have no known competing financial interests or personal relationships that could have appeared to influence the work reported in this paper.

Acknowledgement

This publication is part of the project N19010 in the Partnership Program of the Materials Innovation Institute M2i framework, which is partly financed by the Dutch Research Council (NWO) and the partners Tata Steel and AutomotiveNL. The authors acknowledge C. Kwakernaak and Ruud Hendrikx from the Surfaces & Interfaces group of TU Delft for performing the XRF and EPMA analysis, respectively; Richard Huizenga from X-Ray Facilities Group for XRD measurements. For the Titan TEM results, we also acknowledge support from Frans Tichelaar from the Kavli Institute of Nanoscience, Delft University of Technology, and the Netherlands Electron Microscopy Infrastructure (NEMI), project number 184.034.014, part of the National Roadmap and financed by the Dutch Research Council (NWO).

Appendix A

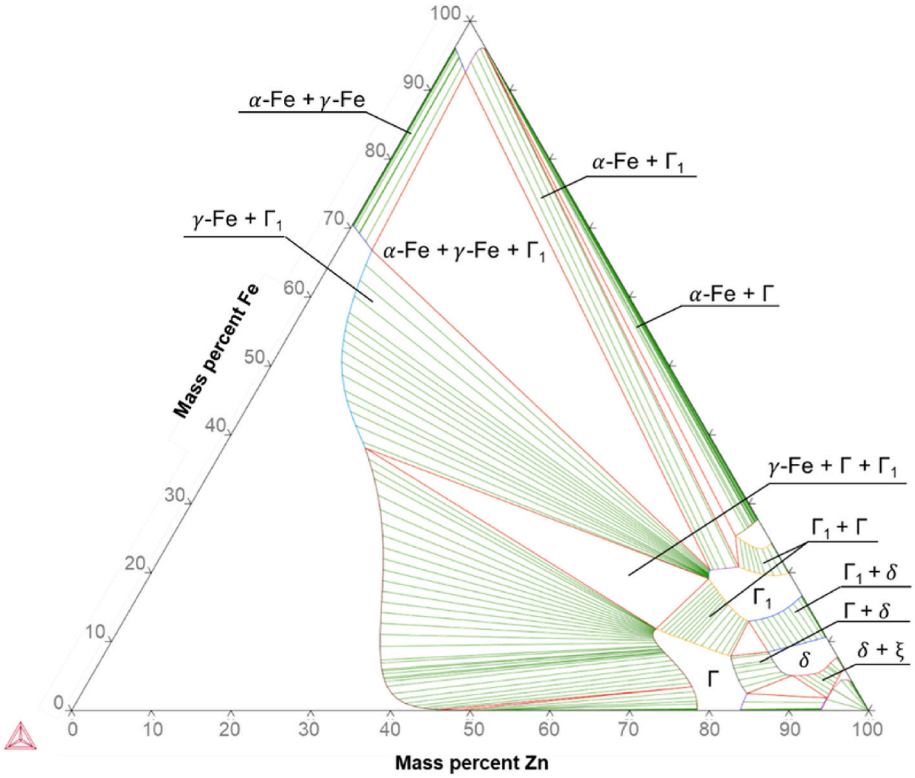

Fig. A1. Equilibrium ternary phase diagram of Fe–Mn–Zn system at 400 °C calculated via ThermoCalc (CALPHAD method). For this calculation, only Fe-based phases and Fe–Zn intermetallics were selected in the database to be represented.

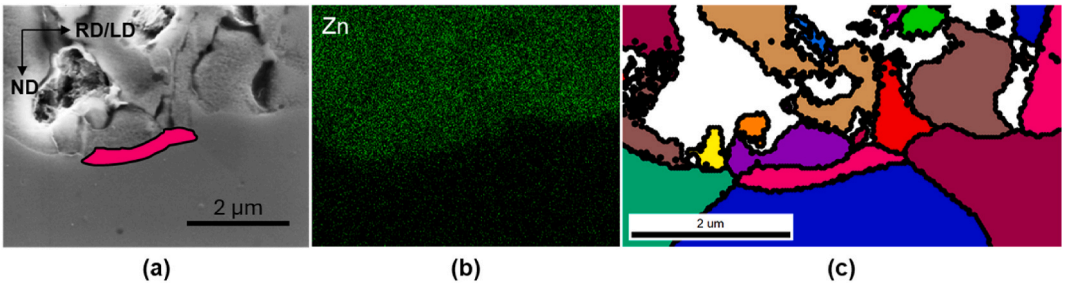

Fig. A2. SEM, Zn EDS map, and unique grain colour map of an area at the tensile specimen's γ-Fe(Zn)/γ-Fe steel substrate boundary interruptedly tested at S3 = 170 MPa and 800 °C. For reference, one of the grains of the unique grain colour map has been illustrated in the SEM image. Black lines in (c) are high-angle grain boundaries.

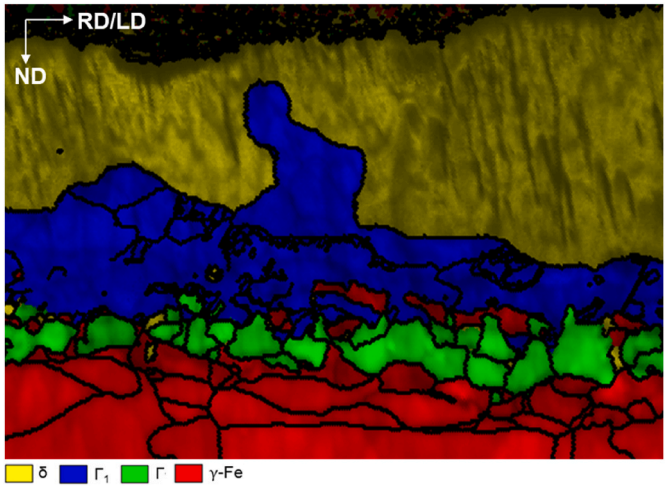

Fig. A3. EBSD phase maps of the interruptedly tested S1 = 90 MPa specimen showing the Fe–Zn intermetallics also observed distributed in irregularly distributed layers.

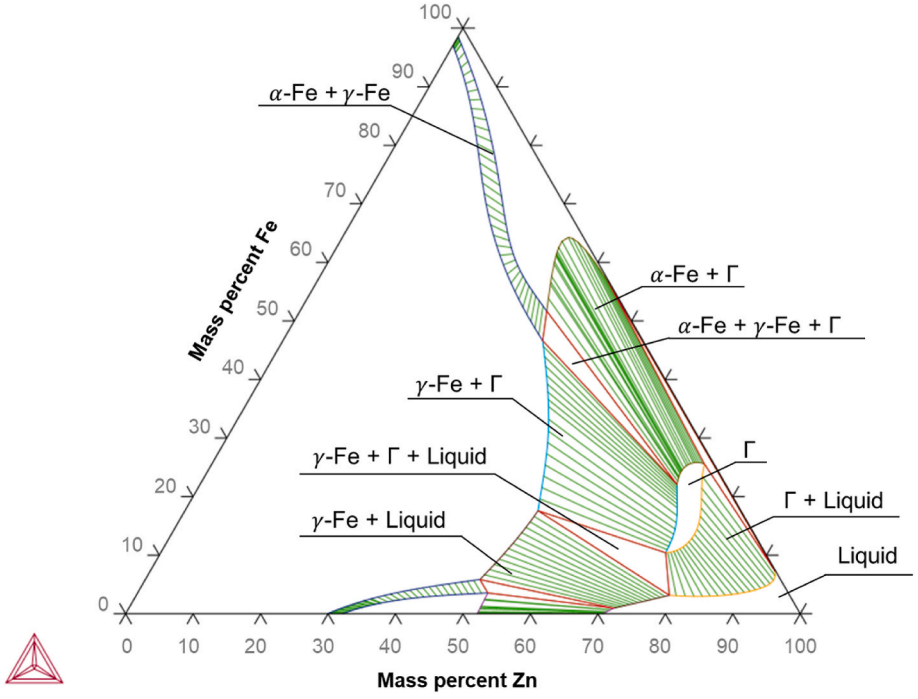

Fig. A4. Equilibrium ternary phase diagram of Fe–Mn–Zn system at 800 °C calculated via ThermoCalc (CALPHAD method). For this calculation, only Fe-based phases and Fe–Zn intermetallics were selected in the database to be represented.

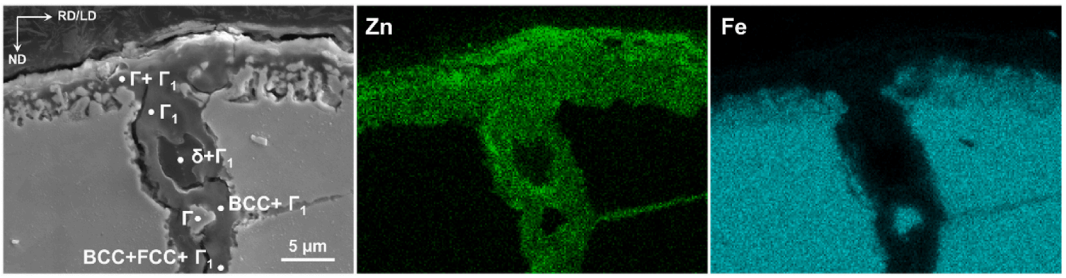

Fig. A5. SEM micrographs and Fe and Zn EDS maps of a crack in the cross-section of the specimen tested up to fracture. In the SEM micrograph, expected phases according to thermodynamically simulations (CALPHAD method), based on elemental content measured by EDS, are identified.

References

[1] Bouaziz O, Allain S, Scott CP, Cugy P, Barbier D. High manganese austenitic twinning induced plasticity steels: a review of the microstructure properties relationships. Curr Opin Solid State Mater Sci 2011;15:141–68. https://doi.org/10.1016/j.cossms.2011.04.002.

[2] Beal C, Kleber X, Fabregue D, Bouzekri M. Embrittlement of a zinc coated high manganese TWIP steel. Mater Sci Eng, A 2012;543:76–83. https://doi.org/10.1016/j.msea.2012.02.049.

[3] Jung G, Woo IS, Suh DW, Kim S-J. Liquid Zn assisted embrittlement of advanced high strength steels with different microstructures. Met Mater Int 2016;22:187–95. https://doi.org/10.1007/s12540-016-5579-7.

[4] Bhattacharya D, Cho L, Van Der Aa E, Pichler A, Pottore N, Ghassemi-Armaki H, et al. Influence of the starting microstructure of an advanced high strength steel on the characteristics of Zn-Assisted liquid metal embrittlement. Mater Sci Eng, A 2021;804:140391. https://doi.org/10.1016/j.msea.2020.140391.

[5] Marié N, Wolski K, Biscondi M. Grain boundary penetration of nickel by liquid bismuth as a film of nanometric thickness. Scr Mater 2000;43:943–9. https://doi.org/10.1016/S1359-6462(00)00518-2.

[6] Ludwig W, Pereiro-López E, Bellet D. In situ investigation of liquid Ga penetration in Al bicrystal grain boundaries: grain boundary wetting or liquid metal embrittlement? Acta Mater 2005;53:151–62. https://doi.org/10.1016/j.actamat.2004.09.012.

[7] Beal C, Kleber X, Fabregue D, Bouzekri M. Liquid zinc embrittlement of twinning-induced plasticity steel. Scr Mater 2012;66:1030–3. https://doi.org/10.1016/j.scriptamat.2011.12.040.

[8] Ling Z, Wang M, Kong L. Liquid metal embrittlement of galvanized steels during industrial processing: a review. In: Chen S, Zhang Y, Feng Z, editors. Trans. Intell. Weld. Manuf. Singapore: Springer Singapore; 2018. p. 25–42. https://doi.org/10.1007/978-981-10-8330-3_2.

[9] Gordon P, An HH. The mechanisms of crack initiation and crack propagation in metal-induced embrittlement of metals. Metall Trans A 1982;13:457–72. https://doi.org/10.1007/BF02643354.

[10] Klinger L, Rabkin E. The effect of stress on grain boundary interdiffusion in a semi-infinite bicrystal. Acta Mater 2007;55:4689–98. https://doi.org/10.1016/j.actamat.2007.04.039.

[11] Stoloff NS, Johnston TL. Crack propagation in a liquid metal environment. Acta Metall 1963;11:251–6. https://doi.org/10.1016/0001-6160(63)90180-9.

[12] Westwood ARC, Kamdar MH. Concerning liquid metal embrittlement, particularly of zinc monocrystals by mercury. Philos Mag 1963;8:787–804. https://doi.org/10.1080/14786436308213836.

[13] Lee H, Jo MC, Sohn SS, Kim S-H, Song T, Kim S-K, et al. Microstructural evolution of liquid metal embrittlement in resistance-spot-welded galvanized twinning-induced plasticity (TWIP) steel sheets. Mater Char 2019;147:233–41. https://doi.org/10.1016/j.matchar.2018.11.008.

[14] Kang H, Cho L, Lee C, De Cooman BC. Zn penetration in liquid metal embrittled TWIP steel. Metall Mater Trans A 2016;47:2885–905. https://doi.org/10.1007/s11661-016-3475-x.

[15] Razmpoosh MH, Biro E, Chen DL, Goodwin F, Zhou Y. Liquid metal embrittlement in laser lap joining of TWIP and medium-manganese TRIP steel: the role of stress and grain boundaries. Mater Char 2018;145:627–33. https://doi.org/10.1016/j.matchar.2018.09.018.

[16] DiGiovanni C, Biro E. A review of current LME test methods and suggestions for developing a standardized test procedure. Weld World 2021;65:865–84. https://doi.org/10.1007/s40194-020-01050-7.

[17] Wright SI, Adams BL. Automatic analysis of electron backscatter diffraction patterns. Metall Trans A 1992;23:759–67. https://doi.org/10.1007/BF02675553.

[18] Wright SI, Nowell MM, Lindeman SP, Camus PP, De Graef M, Jackson MA. Introduction and comparison of new EBSD post-processing methodologies. Ultramicroscopy 2015;159:81–94. https://doi.org/10.1016/j.ultramic.2015.08.001.

[19] Lenthe WC, Singh S, Graef MD. A spherical harmonic transform approach to the indexing of electron back-scattered diffraction patterns. Ultramicroscopy 2019;207:112841. https://doi.org/10.1016/j.ultramic.2019.112841.

[20] Callahan PG, De Graef M. Dynamical electron backscatter diffraction patterns. Part I: pattern simulations. Microsc Microanal 2013;19:1255–65. https://doi.org/10.1017/S1431927613001840.

[21] Belin CHE, Belin RCH. Synthesis and crystal structure determinations in the Γ and δ phase domains of the iron–zinc system: electronic and bonding analysis of Fe13Zn39 and FeZn10, a subtle deviation from the hume–rothery standard? J Solid State Chem 2000;151:85–95. https://doi.org/10.1006/jssc.2000.8626.

[22] Zhu K, Zhu X, Xu R, Tong S, Liang X, Sun X, et al. Effect of rapid heat treatment on mechanical properties and precipitation behavior of medium carbon low alloy steel. J Mater Res Technol 2025;35:5730–45. https://doi.org/10.1016/j.jmrt.2025.02.206.

[23] Álvarez DZ, Bertrand F, Mataigne J-M, Giorgi M-L. Mechanisms and kinetics of the inhibition layer breakdown in the case of Ti IF steel grades galvanized in GA baths. 2015. Toronto, Canada.

[24] Lee CW, Fan DW, Sohn IR, Lee S-J, De Cooman BC. Liquid-metal-induced embrittlement of Zn-Coated hot stamping steel. Metall Mater Trans A 2012;43:5122–7. https://doi.org/10.1007/s11661-012-1316-0.

[25] Zhao J, Ding C, Wu G, Zhang J. Role of aluminum on liquid metal embrittlement susceptibility for Zn–Al–Mg/Sn coated hot-formed steels. J Mater Res Technol 2022;19:747–64. https://doi.org/10.1016/j.jmrt.2022.05.092.

[26] Wu G, Guan C, Tan N, Zhang J. Effect of hot rolled substrate of hydrogen reduction on interfacial reaction layer of hot-dip galvanizing. J Mater Process Technol 2018;259:134–40. https://doi.org/10.1016/j.jmatprotec.2018.04.027.

[27] Janik V, Lan Y, Beentjes P, Norman D, Hensen G, Sridhar S. Zn diffusion and α-Fe (Zn) layer growth during annealing of Zn-Coated B steel. Metall Mater Trans A 2016;47:400–11. https://doi.org/10.1007/s11661-015-3203-y.

[28] Brandes EA, Brook GB, Smithells CJ. In: Brandes EA, Brook GB, editors. Smithells metals reference book. seventh ed. Oxford ; Boston: Butterworth-Heinemann; 1998.

[29] Shewmon P, Abbas M, Meyrick G. Anomalously fast diffusion in the Fe-Zn system. Metall Trans A 1986;17:1523–7. https://doi.org/10.1007/BF02650088.

[30] King AH. Diffusion induced grain boundary migration. Int Mater Rev 1987;32. https://doi.org/10.1179/095066087790150304.

[31] Balluffi RW, Cahn JW. Mechanism for Diffusion Induced Grain Boundary Migration 1981;29:493–500. https://doi.org/10.1016/0001-6160(81)90073-0.

[32] Schmelzle R, Giakupian B, Muschik T, Gust W, Fournelle RA. Diffusion induced grain boundary migration of symmetric and asymmetric ⟨011⟩ {011} tilt boundaries during the diffusion of Zn into Cu. Acta Metall Mater 1992;40:997–1007. https://doi.org/10.1016/0956-7151(92)90077-R.

[33] Oddershede J, Sun J, Gueninchault N, Bachmann F, Bale H, Holzner C, et al. Non-destructive characterization of polycrystalline materials in 3D by laboratory diffraction contrast tomography. Integrating Mater Manuf Innov 2019;8:217–25. https://doi.org/10.1007/s40192-019-00135-6.

[34] Razmpoosh MH, Macwan A, Goodwin F, Biro E, Zhou Y. Role of random and coincidence site lattice grain boundaries in liquid metal embrittlement of iron (FCC)-zn couple. Metall Mater Trans A 2020;51:3938–44. https://doi.org/10.1007/s11661-020-05857-3.

[35] Razmpoosh MH, Macwan A, Goodwin F, Biro E, Zhou Y. Crystallographic study of liquid-metal-embrittlement crack path. Mater Lett 2020;267:127511. https://doi.org/10.1016/j.matlet.2020.127511.

[36] Tumuluru M. Effect of silicon and retained austenite on the liquid metal embrittlement cracking behavior of GEN3 and high-strength automotive steels. Weld J 2019;98. https://doi.org/10.29391/2019.98.029. 351s–64s.

[37] Peng W, Wu G, Zhang J. In-situ observation of liquid zinc-induced erosion behavior diffusion mechanism in zinc-coated 22MnB5 steel. J Mater Res Technol 2020;9:4399–409. https://doi.org/10.1016/j.jmrt.2020.02.064.

[38] Giorgi M-L, Durighello P, Nicolle R, Guillot J-B. Dissolution kinetics of iron in liquid zinc. J Mater Sci 2004;39:5803–8. https://doi.org/10.1023/B:JMSC.0000040092.27463.45.

[39] Marder AR. The metallurgy of zinc-coated steel. Prog Mater Sci 2000;45:191–271. https://doi.org/10.1016/S0079-6425(98)00006-1.

[40] Wang Y, Xing J, Ma S, Zheng B, Liu G, Yang D, et al. Interface characterization and erosion–corrosion behavior of directional Fe-3.5 wt.% B steel in flowing liquid zinc at various temperatures. Corros Sci 2016;104:260–8. https://doi.org/10.1016/j.corsci.2015.12.018.

[41] Allen C, Mackowiak J. A study of the influence of various intermetallic iron-zinc layers on the rates of attack of solid iron by liquid zinc. Corros Sci 1963;3:87–97. https://doi.org/10.1016/S0010-938X(63)80003-7.
[42] Auger T, Vogt J-B, Proriol Serre I. Liquid metal embrittlement. Mech. - microstruct. - corros. Coupling. Elsevier; 2019. p. 507–34. https://doi.org/10.1016/B978-1-78548-309-7.50022-3.
[43] Liu HW. Stress-Corrosion cracking and the interaction between crack-tip stress field and solute atoms. J Basic Eng 1970;92:633–8. https://doi.org/10.1115/1.3425090.
[44] Ikeda Y, Yuan R, Chakraborty A, Ghassemi-Armaki H, Zuo JM, Maaß R. Early stages of liquid-metal embrittlement in an advanced high-strength steel. Mater Today Adv 2022;13:100196. https://doi.org/10.1016/j.mtadv.2021.100196.